
Article:
Yang, F. orcid.org/0000-0002-6428-7755, Wu, P. and Sinclair, D. (2017) Suppression of electrical conductivity and switching of conduction mechanisms in 'stoichiometric' (Na0.5Bi0.5TiO3)1-x(BiAlO3)x (0 ≤ x ≤ 0.08) solid solutions. Journal of Materials Chemistry C. ISSN 2050-7526

https://doi.org/10.1039/C7TC02519J

Journal of
Materials Chemistry C

Accepted Manuscript

This article can be cited before page numbers have been issued, to do this please use: F. Yang, P. Wu and D. Sinclair, *J. Mater. Chem. C*, 2017, DOI: 10.1039/C7TC02519J.

ROYAL SOCIETY OF CHEMISTRY

rsc.li/materials-c

View Article Online
DOI: 10.1039/C7TC02519J

Journal Name

ARTICLE

Suppression of electrical conductivity and switching of conduction mechanisms in 'stoichiometric' $(Na_{0.5}Bi_{0.5}TiO_3)_{1-x}(BiAlO_3)_x$ ($0 \le x \le 0.08$) solid solutions

Received 00th January 20xx,
Accepted 00th January 20xx

DOI: 10.1039/x0xx00000x

www.rsc.org/

F. Yang,[a,] † P. Wu[a] and D. C. Sinclair[a,] †

$(Na_{0.5}Bi_{0.5}TiO_3)_{1-x}(BiAlO_3)_x$ ($0 \le x \le 0.08$) solid solutions were prepared by solid state reaction and their electrical properties established by *ac* impedance spectroscopy and electromotive force transport number measurements. Incorporation of $BiAlO_3$ (BA) decreases the electrical conductivity of $Na_{0.5}Bi_{0.5}TiO_3$ (NBT) and with increasing *x* sequentially changes the conduction mechanism from predominant oxide-ion conduction, to mixed ionic-electronic conduction and finally to predominant electronic conduction. The suppressed oxide-ion conduction by BA incorporation significantly reduces the dielectric loss at elevated temperatures and produces excellent high-temperature dielectric materials for high BA contents. Possible reasons for the suppressed oxide-ion conduction in the NBT-BA solid solutions are discussed and we propose the local structure, especially trapping of the oxygen vacancies by Al^{3+} on the B-site, plays a key role in the oxide-ion conduction in these apparently 'stoichiometric' NBT-based solid-solution perovskite materials.

Introduction

Sodium bismuth titanate, $Na_{0.5}Bi_{0.5}TiO_3$ (NBT), is considered a promising lead-free piezoelectric/ferroelectric material to replace lead zirconate titanate (PZT) because of its high Curie temperature (T_c ~ 325 °C), relatively high remnant polarization (P_r =38 μC cm^{-2}) and piezoelectric constant (d_{33} = 73 pC N^{-1}).[1-3] NBT was first reported in the 1960s and has received increasing attention in recent years driven by the surge in developing lead-free materials.[4] One major drawback of NBT as a piezoelectric/dielectric material can be its high electrical conductivity which leads to high dielectric loss (tan δ) and leakage currents at elevated temperatures.[1] Many studies have been carried out to modify the electrical properties of NBT by forming solid solutions with other perovskites,[5-13] among which the NBT-$BiAlO_3$ system was reported to present excellent ferroelectric and piezoelectric properties compared with NBT.[12,13]

$BiAlO_3$ (BA) is a relatively new high T_c lead-free ferroelectric material.[14-16] Its large ferroelectric polarization and piezoelectricity were first predicted using density functional theory by Baettig *et al*. [14] and later confirmed by experiments.[15,16] $BiAlO_3$ has a rhombohedral perovskite-type structure at room temperature with Al^{3+} on an octahedral site. It has a T_c > 520 °C, d_{33} = 28 pC N^{-1}, P_r = 9.5 μC cm^{-2} at room temperature which increases to 26.7 μC cm^{-2} at 225 °C.[15] $BiAlO_3$ can only be prepared under high pressure (e.g., 6 GPa) and it decomposes around 550 °C; however, it can be partially stabilized by forming solid solutions with other perovskite materials such as $BaTiO_3$ [17] and NBT [12, 13, 18, 19] to modify the structure and properties of the host.

$(NBT)_{1-x}(BA)_x$ solid solutions have been studied by several researchers. Yu and Ye [12] reported the NBT-BA system can remain single phase up to x = 0.08. They found incorporation of BA into NBT enhanced P_r and d_{33}, decreased *E*c and significantly reduced the dielectric loss at elevated temperatures. Watanabe *et al.* [18] also reported a solid solution limit of 8% for BA in NBT and an increased d_{33} with increasing x. Ullah *et al.* [13] reported optimised ferroelectric and piezoelectric properties at x = 0.05 and a rhombohedral to pseudocubic phase transition at x = 0.075. Manotham *et al.* [19] compared the properties of $(NBT)_{0.94}(BA)_{0.06}$ ceramics prepared by two-step sintering and conventional sintering. Peng *et al.* [20] combined results from dielectric measurements and transmission electron microscopy to suggest co-existence of ferroelectric and anti-ferroelectric phases in $(NBT)_{0.92}(BA)_{0.08}$ ceramics. The above studies focus mainly on the improvement of ferroelectric/piezoelectric properties of NBT by BA incorporation. There is little information about the effect of BA on the electrical conductivity and conduction mechanism of NBT, which are critical to the dielectric loss and leakage current of NBT. [21-23]

Our previous studies have shown that NBT displays a variety of electrical behaviour.[21-24] The nominally stoichiometric NBT (nominal $Na_{0.5}Bi_{0.5}TiO_3$; $NB_{0.50}T$), presents high conductivity with an oxide-ion transport number t_{ion} ~ 0.9 at 600 - 800 °C. As t_{ion} is the fraction of the total current carried by oxygen ions, such a high t_{ion} suggests the electrical conduction is dominated by oxygen ions. The predominance of oxide-ion conduction (as opposed to sodium ion or electronic conduction) in $NB_{0.50}T$ has been further confirmed by ^{18}O tracer diffusion measurements. The high oxide-ion conductivity in $NB_{0.50}T$ is attributed to

[a.] *Department of Materials Science & Engineering, University of Sheffield, Mappin Street, Sheffield, S1 3JD, United Kingdom.*
† Corresponding authors. fan.yang@sheffield.ac.uk; d.c.sinclair@sheffield.ac.uk

View Article Online
DOI: 10.1039/C7TC02510J

oxygen vacancies generated through low levels of Bi_2O_3 loss during ceramic processing according to the Kroger-Vink equation,

$$2Bi_{Bi}^{x} + 3O_{O}^{x} \rightarrow 2V_{Bi}^{'''} + 3V_{O}^{\bullet\bullet} + Bi_2O_3 \quad (1)$$

as well as the high oxygen ion mobility associated with highly polarized Bi^{3+} ions and weak Bi-O bonds.[25] Bi-deficient NBT (nominal $Na_{0.5}Bi_{0.49}TiO_{2.985}$; $NB_{0.49}T$) presents higher conductivity with $t_{ion} > 0.9$ due to generation of additional oxygen vacancies. In contrast, the oxide-ion conductivity is suppressed in Bi-excess NBT ($Na_{0.5}Bi_{0.51}TiO_{3.015}$; $NB_{0.51}T$) as the excess Bi_2O_3 in $NB_{0.51}T$ can compensate for Bi_2O_3 loss during processing, thus $NB_{0.51}T$ exhibits low levels of electronic conduction with an activation energy of ~ 1.6 eV which is close to half of the band gap of NBT.[26] The predominant electronic conduction in $NB_{0.51}T$ is confirmed by a $t_{ion} < 0.1$ at 600- 800 °C. Later work shows a further increase in the starting Bi-excess content (for example, $Na_{0.5}Bi_{0.52}TiO_{3.03}$; $NB_{0.52}T$) can reintroduce oxide-ion conductivity into NBT. $NB_{0.52}T$ shows mixed conduction behaviour with comparable contributions from oxide-ion conduction and electronic conduction showing a t_{ion} close to 0.5, which is possibly linked to a change in the Bi-content in the NBT main phase or a space charge effect because of the presence of a Bi-rich secondary phase.[23]

Mixed ionic-electronic conduction followed by low levels of electronic conduction and therefore excellent high temperature dielectric behaviour was also observed for Nb-doped NBT. This study was based on Nb-replacing Ti on the B-sites with incorporation of the excess oxygen 'filling' the oxygen vacancies associated with Bi_2O_3 loss during processing.[23] Based on the magnitude of bulk conductivity, σ_b and t_{ion} values, we concluded that undoped NBT and Nb-doped NBT can exhibit three types of electrical behaviour: Type I, predominant oxide-ion conduction, high σ_b, t_{ion} ~ 0.9; Type II, mixed ionic-electronic conduction, intermediate σ_b, t_{ion} ~ 0.5; Type III, predominant electronic conduction, low σ_b, $t_{ion} < 0.1$. These three types of electrical behaviour can be clearly distinguished from the tanδ-T relationship (measured at 1 MHz). Type I NBT shows a sharp rise of tanδ with increasing temperature and tanδ exceeds 0.2 at ~ 350 °C. In contrast, Type III presents low tanδ in a wide temperature range (< 0.02 from 300 to 600 °C), making it an excellent high-temperature dielectric material. In between Type I and III, Type II shows low tanδ in a narrow temperature range and a steep rise above ~ 500 °C to exceed 0.1 at 600 °C.

The above findings not only reveal the electrical conduction mechanisms of NBT but also show the flexibility in tailoring the properties of NBT for various applications such as piezoelectric/dielectric devices, oxide-ion conductors and mixed ionic-electronic conductors. Here, the electrical conductivity and conduction mechanism of $(NBT)_{1-x}(BA)_x$ ($0 \le x \le 0.08$) solid solutions were studied by impedance spectroscopy and electromotive force measurements. The purpose is not only to investigate the effect of BA on the electrical conductivity of NBT, but also to further understand the factors that control the oxide-ion conduction in NBT to tailor its electrical properties. The results show that BA incorporation decreases the electrical conductivity of NBT and changes the conduction mechanism from predominant oxygen-ion conduction to ionic-electronic mixed conduction and then to predominant electronic conduction with increasing BA content. The suppressed conductivity and changes in conduction mechanisms significantly reduces the dielectric loss at elevated temperatures to make NBT an excellent high-temperature dielectric material. This study provides an alternative approach to fine-tune the electrical properties of NBT as opposed to manipulating the A-site Na/Bi non-stoichiometry in undoped materials or by B-site Nb donor doping.

Experimental

$(Na_{0.5}Bi_{0.5}TiO_3)_{1-x}(BiAlO_3)_x$ ($0 \le x \le 0.08$) solid solutions were prepared by a solid state reaction method using Na_2CO_3 (99.5%, Fisher chemical, UK), Bi_2O_3 (99.9%, Acros Organics, USA), TiO_2 (99.9%, Sigma Aldrich, UK) and Al_2O_3 (99.95%, Alfa Aesar, UK) as starting materials. Prior to weighing, the raw powders were dried overnight at 300 °C for Na_2CO_3 and Bi_2O_3, 800 °C for TiO_2 and 900 °C for Al_2O_3. Appropriate amounts of each precursor were weighed and mixed thoroughly in iso-propanol using yttria-stabilised zirconia grinding media for 6 h. The mixture was dried at 85 °C overnight, sieved and calcined at 850 °C for 2 h. The resultant powder was subjected to a second round of ball milling, drying, sieving and calcined at 900 °C for 2 h. After a third round of milling, drying and sieving, the final powder was compacted into pellets by uni-axial cold pressing followed by isostatical pressing at 200 MPa. Pellets were embedded in sacrificial powder of the same composition and sintered at 1175 °C for 2 h in air. For pure NBT, powder was calcined at 800 °C twice and the pellet was sintered at 1150 °C. After sintering, pellets were ground on SiC sand paper to remove the sacrificial powder. Pellets ~ 0.85 cm in diameter and ~ 0.15 cm in thickness were used for impedance and LCR measurements.

Ceramic density was measured by the Archimedes' method and compared to the theoretical X-ray density. Phase purity was examined by X-ray diffraction on crushed pellets using a high resolution STOE STADI-P diffractometer (STOE & Cie GmbH, Darmstadt, Germany) operating with $CuK\alpha_1$ radiation with a linear position-sensitive detector. Before measurement the crushed pellets were annealed at 400 °C for 4 h to eliminate any residual stress caused by crushing and grinding. Structural refinement was carried out for reflections in the range of $20° \le 2\theta \le 80°$ using EXPGUI.[27, 28] Ceramic microstructures were observed by scanning electron microscopy on thermally-etched surfaces using a Philips XL30 SEM. Compositions were obtained by energy dispersive X-ray spectroscopy (EDS) on carbon-coated polished surfaces (without thermal etch). Raman spectroscopy measurements were carried out using a 514 nm Ar laser line in a Renishaw inVia Raman microprobe system.

Electrical properties of the pellets were obtained from *ac* impedance spectroscopy using an Agilent E4980A impedance analyser (Agilent Technologies Inc., Palo-Alto, CA; frequency range: 1 MHz to 20 Hz) and/or a Solarton 1260 system (Solartron Analytical, UK; frequency range 1 MHz to 0.1 Hz). Before measurements, Au paste was painted to cover both surfaces of the pellets and then fired at 800 °C for 2 h to serve

View Article Online
DOI: 10.1039/C7TC02519J

as electrodes. Impedance measurements were carried out in flowing N_2, air and O_2 from 400 - 800 °C at increments of 50 °C. The equilibrium time between each measurement was 30 minutes. Equivalent circuit fitting was performed using ZView software (Scribner Associates, Inc, Southern Pines, NC). Dielectric properties were measured using an LCR meter (Agilent E4980 Precision LCR Meter, Agilent Technologies) with an applied ac voltage of 100 mV. Data points were collected every 60 s from room temperature (RT) to 800 °C using a non-inductively wound tube furnace at a ramping rate of 1 °C min^{-1}. Oxygen-ion transport number measurements were performed using a Probostat system (NorECs Norwegian Electro Ceramics AS, Oslo, Norway). A sample, ~ 1.7 cm in diameter and ~ 0.2 cm in thickness, was sealed onto an YSZ tube using a commercial glass frit. Before that, Pt electrodes, ~ 1.0 cm in diameter, were coated in the centre of the pellet surfaces and fired at 900 °C for 2 h. An oxygen partial pressure (pO_2) difference was created across the ceramic by flowing N_2 into the YSZ tube and leaving the outside of the ceramic in air. The pO_2 difference was monitored by measuring the voltage across the inner and outer electrodes on the YSZ tube. The voltage was measured using a Keithley 182 sensitive digital voltmeter. More details of transport number measurement can be found in ref.21.

Results

Phase, composition and microstructure

The $(NBT)_{1-x}(BA)_x$ ($0 \le x \le 0.08$) solid solutions are phase-pure based on XRD, Fig. 1a. An expanded view of the 2θ range between 38 and 42° shows the superlattice reflection from a rhombohedral structure for all compositions, Fig. 1b. The structure could be refined to a rhombohedral cell (space group R3*c*), Fig. 1c. The pseudo-cubic cell volume decreases with increasing *x*, Fig. 1d. The relative density of sintered ceramics was > 95%, as listed in Table 1.

Although phase-pure by XRD, SEM micrographs of polished surfaces of x = 0.07 and 0.08 showed the presence of small amounts of an Al-rich secondary phase, Fig. 2a and 2b. EDS analysis on the solid solutions shows the atomic fractions of the A-site (Na, Bi) cations are close to their nominal values, Fig. 2c; the atomic fraction of Al^{3+} on B-site slightly deviates from its nominal value for x = 0.07 and 0.08 because of the presence of the Al-rich secondary phase, Fig. 2d.

A typical SEM micrograph of thermally-etched surfaces of the solid solutions is shown in Fig. 3a. Average grain size of the solid solutions decreases with increasing *x*, from ~ 10 µm for x = 0.01 to ~ 1.5 µm for x = 0.08, Fig. 3b. Undoped NBT has smaller grains compared to x = 0.01 and 0.02, which may be due to the lower sintering temperature (1150 °C) compared to 1175 °C for the solid solutions.

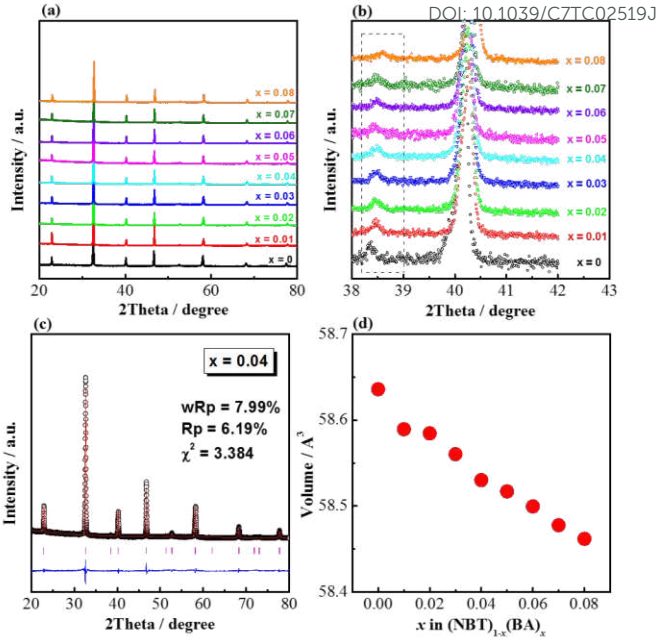

Fig. 1 (a) Room-temperature XRD patterns of $(NBT)_{1-x}(BA)_x$ ($0 \le x \le 0.08$) solid solutions; (b) an expand view of the 2θ range between 38 and 42° showing the superlattice reflection of the rhombohedral structure in the rectangle. (c) Rietveld refinement of the XRD pattern (as an example) of the solid solution member x = 0.04. The open symbols represent the observed pattern and the solid line shows the calculated fit. The reflection marker for the R3*c* structure is shown as vertical lines with the difference pattern below the diffraction pattern. The quality of fit is indicated in the figure. (d) Pseudo-cubic cell volume as a function of *x*. Error bars are within the symbols.

Table 1. Theoretical, experimental and relative density of sintered $(NBT)_{1-x}(BA)_x$ ($0 \le x \le 0.08$) ceramics.

Composition x	Density		
	Theoretical (g cm^{-3})	Experimental (g cm^{-3})	Relative (%)
0	6.00	5.72	95.3
0.01	6.03	5.91	98.0
0.02	6.05	5.98	98.8
0.03	6.07	5.95	98.0
0.04	6.09	5.88	96.6
0.05	6.12	5.99	97.9
0.06	6.14	5.87	95.6
0.07	6.16	6.06	98.4
0.08	6.18	5.87	95.0

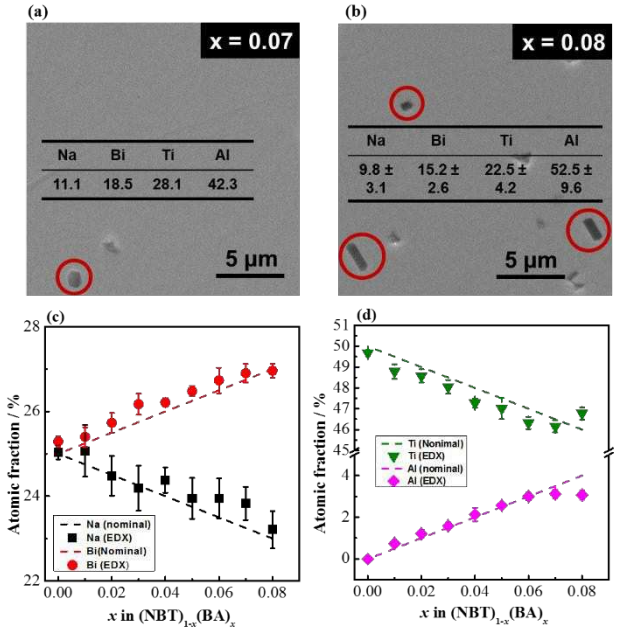

Fig.2 (a) and (b) SEM micrographs of polished surfaces of x = 0.07 and 0.08 showing the presence of a secondary phase (indicated by the red circles); the inset table lists the atomic percentage of cations from the secondary phase obtained from EDS analysis. (c) and (d) atomic fraction of A-site (Na, Bi) and B-site (Ti, Al) cations obtained from EDS, respectively. Data were collected from 5 randomly selected areas on polished surfaces (without thermal etching).

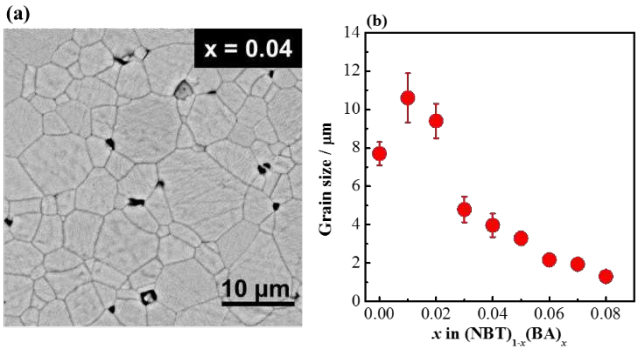

Fig.3 (a) A typical SEM micrograph of a thermally-etched surface of a $(NBT)_{1-x}(BA)_x$ ($0 \le x \le 0.08$) solid solution member (x = 0.04 as an example); (b) average grain size as a function of x. Grain size of each composition was obtained by counting the number of grains across the diagonal. Error bars were from 5 micrographs.

Raman spectroscopy

Room-temperature Raman spectra of $(NBT)_{1-x}(BA)_x$ ($0 \le x \le 0.08$) solid solutions are shown in Fig. 4a. The spectrum of NBT is consistent with previous reported data [29-32] and the spectra of NBT-BA solid solutions show similar features, where broad bands are observed due to A-site Na/Bi disorder and overlapping Raman modes. Between 100 and 1000 cm^{-1}, there are four main regions, from low to high wavenumber, attributing to Na-O (~ 135 cm^{-1}), Ti-O (~ 280 cm^{-1}) and TiO_6 octahedral (400 – 1000 cm^{-1}) vibrations/rotations, respectively. The spectra can be de-convoluted into eight peaks using Lorentzian functions, and the evolution of the peak positions of the main modes as a function of x is shown in Fig. 4b. There is no clear frequency shift of the Na-O band with increasing x; whereas the Ti-O and TiO_6 octahedral bands show a systematic shift to higher frequency with increasing x. Raman frequency, ω, is determined by $\omega = \sqrt{k/\mu}$, where k is the force constant and μ is the reduced mass based on the harmonic oscillator approximation. The ionic radius of Al^{3+} (0.535 Å, 6-fold co-ordination) is smaller than that of Ti^{4+} (0.605 Å, 6-fold co-ordination), resulting in a shorter bond length and thus a higher force constant k. [33] The relative atomic mass of Al (26.98) is also lower than Ti (47.87). Because of the smaller ionic size and atomic mass of Al, the Ti-O band is shifting to higher frequency with increasing x. The TiO_6 octahedral bands are dominated by vibrations involving mainly oxygen displacement and thus are expected to be unaffected by the mass of the cations. The shift to higher frequency of these bands is due to an increased force constant k caused by the smaller ionic size of Al^{3+}. Raman spectra further confirm the formation of NBT-BA solid solutions, and the Ti-O band shift to high frequency gives evidence that Al^{3+} goes to Ti-site of NBT as desired.

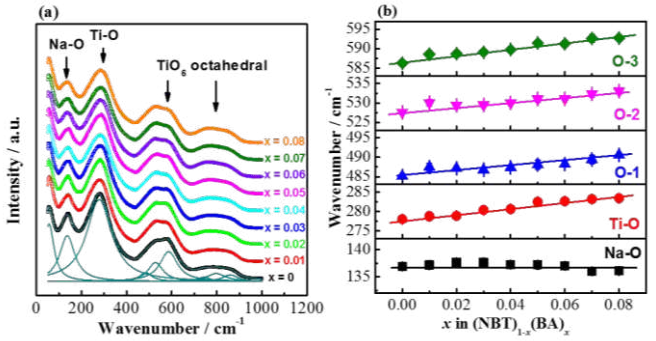

Fig. 4 (a) Room-temperature Raman spectroscopy of $(NBT)_{1-x}(BA)_x$ ($0 \le x \le 0.08$) solid solutions and the spectral deconvolution of Raman spectrum of NBT; (b) evolution of Raman peaks near 120, 280, 480, 525 and 580 cm^{-1} as a function of x. The solid lines show the trend.

Electrical properties

Complex impedance plane (Z*) plots of $(NBT)_{1-x}(BA)_x$ ($0 \le x \le 0.08$) solid solutions measured at 600 °C are shown in Fig. 5a-5c. Z* plot for NBT shows three well-resolved arcs (inset of Fig. 5a), from high to low frequency, corresponding to responses from bulk, grain boundary and electrode effect, respectively. This is consistent with our previous report.[21, 23] For the NBT-BA

View Article Online
DOI: 10.1039/C7TC02510J

solid solutions, Z* plots show the following evolution with increasing BA concentration: 1) The magnitude of impedance, both for the bulk and grain boundary regions, increases with increasing *x*; 2) the two responses from the bulk and grain boundary become less well resolved with increasing *x* ($0.01 \le x \le 0.05$) and eventually merge into a single arc for $x \ge 0.06$. The associated capacitance of the single arc is ~ 7×10^{-11} F cm^{-1}, corresponding to a relative permittivity (ε_r) of ~ 800, which agrees with the value for paraelectric NBT materials at this temperature. Therefore, the single arc in the Z* plots for $x \ge 0.06$ represents the bulk response. The decreasing resolution for the two arcs on Z* plots for $0.01 \le x \le 0.05$ is attributed to the closer time constant (τ) for the bulk and the grain boundary components with increasing *x*. The impedance data are also presented as M''-log*f* spectroscopic plots, Fig. 5d. M, the electric modulus and its complex form is defined as $M^* = j\omega C_0 Z^*$, where ω is the angular frequency, C_0 is the capacitance of an empty cell and Z* is the complex impedance. For easy comparison, M'' (the imaginary component of M*) was normalized to its peak maximum and it shows a systematic peak shift to lower frequency with increasing *x*. The M'' peak position, $f_{max} = 1/(2\pi RC)$ is an intrinsic property of a material. As *C* does not show significant change with composition, a peak shift to lower frequency indicates a decrease in conductivity (and therefore an increases in resistance).

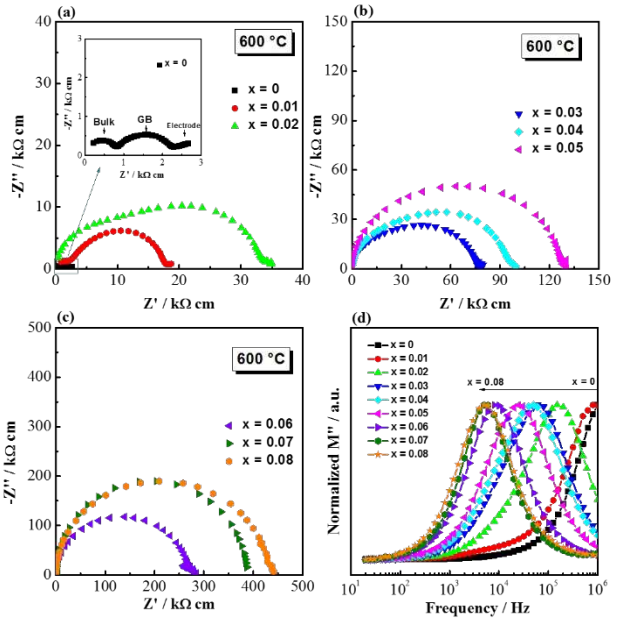

Fig. 5 Impedance spectroscopy of $(NBT)_{1-x}(BA)_x$ ($0 \le x \le 0.08$) solid solutions measured at 600 °C in the frequency range from 1 MHz to 20 Hz. (a)-(c) Z* plots. The inset figure in (a) is an expanded view of $x = 0$. (d) M''-log*f* spectroscopic plots; M'' data were normalized to the peak maximum to illustrate the peak shift to lower frequency.

For $0 \le x \le 0.02$, the relatively well-resolved impedance spectra were fitted by an equivalent circuit of three series-connected R-CPE elements to obtain the resistances R_b, R_{gb} and R_{tot} ($R_{tot} = R_b + R_{gb}$). For $0.03 \le x \le 0.08$, the bulk resistance was calculated from the M'' peak frequency and peak maximum, and the total resistance was obtained from the Z' intercept on Z* plots. This is to avoid large errors from equivalent circuit fitting due to the less well-resolved impedance responses from the bulk and grain boundary components. R_b and R_{tot} were converted to σ_b (= $1/R_b$) and σ_{tot} (= $1/R_{tot}$) and presented in Arrhenius plots, Fig. 6, where systematic decreases of σ_b and σ_{tot} with increasing *x* can be observed.

Activation energies (E_a) for σ_b and σ_{tot} are listed in Table 2. For σ_b, there is a notable change in the activation energy (Ea) with increasing *x*, from << 1 eV for $0 \le x \le 0.02$, ~ 1.2 eV for $x = 0.04$, 0.05 and to > 1.6 eV for $0.06 \le x \le 0.08$. Ea for σ_{tot} also increases with *x*, from ~ 0.9 eV for $x = 0$, 1.3 - 1.5 eV for $0.01 \le x \le 0.05$ to to > 1.6 eV for $0.06 \le x \le 0.08$.

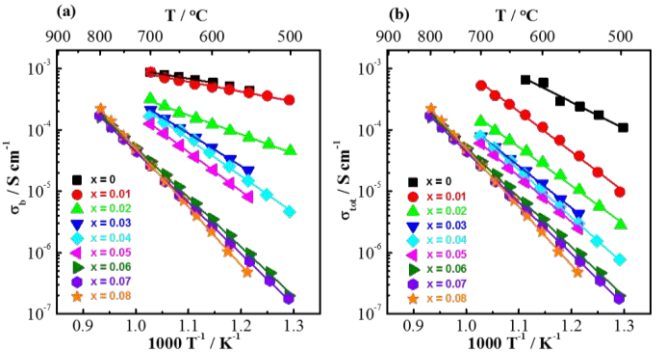

Fig. 6 Arrhenius plots for (a) bulk conductivity and (b) total conductivity of the $(NBT)_{1-x}(BA)_x$ ($0 \le x \le 0.08$) solid solutions measured in air.

Table 2. Activation energies, E_a, for bulk conductivity and total conductivity of the $(NBT)_{1-x}(BA)_x$ ($0 \le x \le 0.08$) solid solutions.

Composition *x*	E_a (eV)	
	Bulk	Total
0	0.31 ± 0.03	0.87 ± 0.08
0.01	0.32 ± 0.02	1.31 ± 0.03
0.02	0.63 ± 0.02	1.26 ± 0.03
0.03	1.07 ± 0.01	1.37 ± 0.01
0.04	1.21 ± 0.03	1.54 ± 0.01
0.05	1.28 ± 0.01	1.48 ± 0.01
0.06	1.62 ± 0.02	1.62 ± 0.02
0.07	1.67 ± 0.01	1.67 ± 0.01
0.08	1.90 ± 0.01	1.90 ± 0.01

Fig.7 shows the impedance spectra measured in flowing nitrogen, air and oxygen for selected compositions showing the

effect of pO_2. For x = 0.01, the bulk response does not change with pO_2, as shown by the inset in Fig.7a and the overlapping peaks in the M''-log$f$ spectroscopic plots, Fig. 7b. This suggests that the bulk conduction is dominated by ionic species. The grain boundary impedance is dependent on pO_2: it is lowest in N_2 and largest in O_2, indicating the presence of n-type electronic conduction. It is also noteworthy that the low frequency electrode spike is most prominent in N_2 and least prominent in O_2, suggesting the presence of oxide-ion conduction. For x = 0.06, Z* plots show the smallest single arc in N_2 and the largest arc in O_2, Fig. 7c and M''-log$f$ spectroscopic plots show a peak shift towards high frequency in N_2, Fig. 7d. The low frequency electrode spike is still present in N_2, as shown in the inset in Fig. 7c. The pO_2-dependent impedance and the low frequency spike suggest a mixed ionic-electronic conduction mechanism. Conducting species are electrons and oxygen ions. For x = 0.07, Z* (Fig. 7e) and M''-log$f$ (Fig. 7f) plots show similar pO_2-dependence as x = 0.06, however, the low frequency electrode spike is less apparent (inset of Fig.7e). This suggests the bulk conduction is dominated by an n-type electronic conduction mechanism.

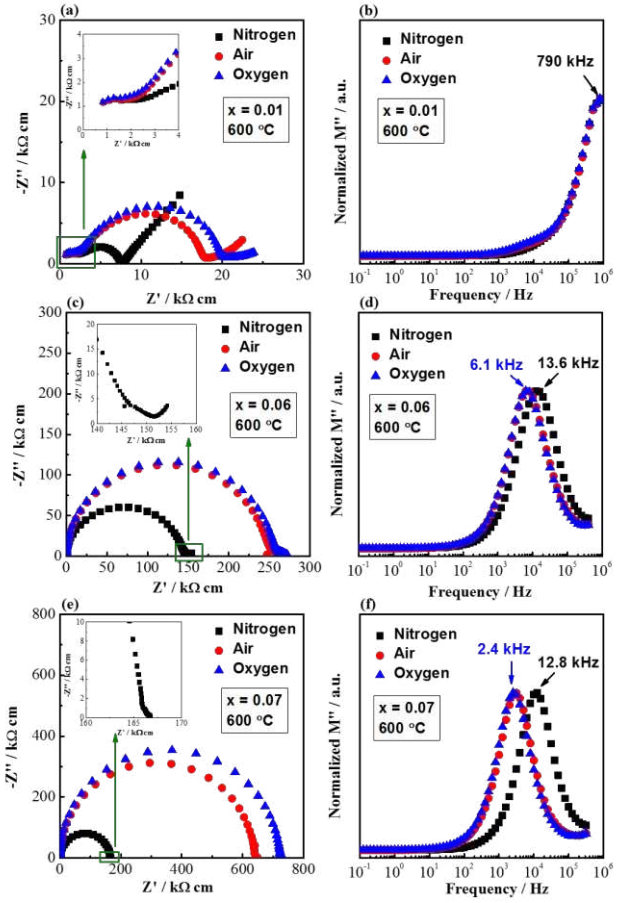

Fig.7 Impedance spectroscopy of $(NBT)_{1-x}(BA)_x$ ($0 \le x \le 0.08$) solid solutions at 600 °C in flowing nitrogen, air and oxygen in the frequency range from 1 MHz to 0.1 Hz. (a), (c) and (e) Z* plots for x = 0.01, 0.06 and 0.07, respectively. Inset in each figure is an expanded view of the region in the rectangle. (b), (d) and (f): M''-log$f$ spectroscopic plots for x = 0.01, 0.04 and 0.07, respectively. The numbers inside each figure indicate the frequency at the M'' maxima.

Oxygen-ion transport number, t_{ion}, at 600 °C for selected compositions of x is shown in Fig. 8. t_{ion} drops from > 0.9 for NBT (x = 0), 0.4 – 0.8 for $0.02 \le x \le 0.06$ and to < 0.1 for x = 0.07. This agrees with the information extracted from Fig. 7. According to the classification proposed in our previous study,[23] the electrical conduction of NBT-BA solid solutions also displays three types of behaviour: Type I: t_{ion} > 0.85, predominant oxide-ion conduction; Type II, $0.15 \le t_{ion} \le 0.85$, mixed ionic-electronic conduction; Type III, t_{ion} < 0.15, electronic conduction. Incorporation of BA into NBT is an alternative approach to tune the electrical conduction mechanism and conductivity of NBT-based materials as opposed to solely manipulating the A-site nonstoichiometry (Na/Bi ratio) or B-site Nb doping.[23]

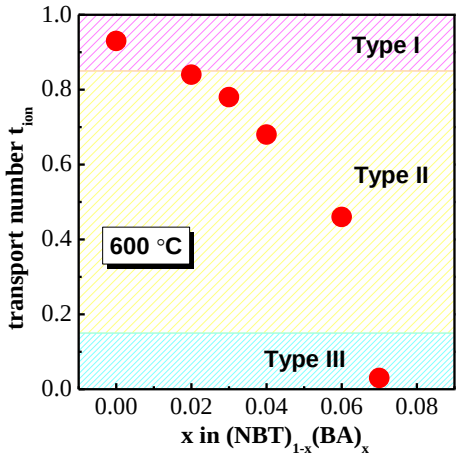

Fig. 8 Oxygen-ion transport number at 600 °C as a function of x.

Dielectric properties

The permittivity-temperature (ε_r – T) profiles for selected compositions of the NBT-BA solid solutions are shown in Fig. 9a. The permittivity maximum decreases slightly with increasing x, from ~ 3000 for NBT to ~ 2700 for x = 0.07. The temperature where permittivity shows its maximum, T_m, also decreases with increasing x, from ~ 325 °C for NBT to ~ 290 °C for x = 0.07. Incorporation of BA into NBT has a much more significant effect on the dielectric loss-temperature profile, Fig. 9b. NBT (x = 0) shows a sharp rise of tanδ with increasing temperature and tanδ exceeds 0.2 at ~ 350 °C. In contrast, x = 0.07 exhibits very low tanδ over a wide temperature range (< 0.02 from 300 to 700 °C). Compositions in between x = 0 and 0.07 show low tanδ in a narrower temperature range and a steep rise above ~ 600 °C, exceeding 0.1 at 650 °C.

View Article Online
DOI: 10.1039/C7TC02540J

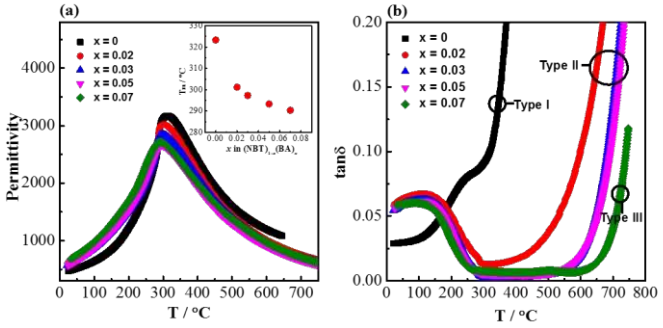

Fig. 9 Dielectric spectroscopy for selected compositions of $(NBT)_{1-x}(BA)_x$ ($0 \le x \le 0.08$) solid solutions: (a) permittivity at 1 MHz versus temperature. The inset figure shows the change of T_m as function of *x*. (b) Dielectric loss (1MHz) versus temperature. Type I, II and III behaviour as defined in ref. [23].

Discussion

The electrical conductivity of $(NBT)_{1-x}(BA)_x$ ($0 \le x \le 0.08$) solid solutions decreases with increasing *x* and the conduction mechanism changes from predominant oxygen-ion conduction via ionic-electronic mixed conduction to predominant electronic conduction with a continuous drop of t_{ion} from > 0.9 for $x = 0$ to < 0.1 for $x = 0.07$. Incorporation of BA into NBT suppresses the oxide-ion conduction in NBT and makes it an excellent high-temperature dielectric material. Possible reasons for the suppressed oxide-ion conduction are discussed below.

For a single type of charge carriers, the electrical conductivity is determined by $\sigma = cq\mu$, where *c*, *q* and μ are the concentration, charge and mobility of the charge carriers, respectively. As the oxide-ion conduction is suppressed by BA incorporation, there is either a decrease in the concentration and/or a decrease in the mobility of the oxygen vacancies.

The oxide-ion conductivity of NBT originates from the oxygen vacancies generated through a small amount of Bi_2O_3-loss during ceramic processing as described by Equation 1. Our previous study [24] showed that 0.5-1% donor (Nb) doping on B-site of NBT can fill up the oxygen vacancies and significantly decrease the electrical conductivity. Therefore, the oxygen vacancy concentration in NBT is estimated to be in the range of 0.25 - 0.5%, corresponding to a Bi_2O_3-loss of 0.17 - 0.33%. Such a small loss of Bi_2O_3 is "accidental" and therefore difficult to control in a reproducible manner.[24] With BA incorporation into NBT, the defect chemistry can be described by the following Kroger-Vink equation:

$$Na_A^x + Bi_A^x + 2Ti_{Ti}^x + 6O_O^x \xrightarrow{2BiAlO_3} Bi_A^{\bullet\bullet} + Bi_A^x + 2Al_{Ti}^{'} + 6O_O^x, \quad (2)$$

where we have used the subscript A to denote the disorder of the Na and Bi ions on the A-site of the NBT lattice. Incorporation of BA into NBT does not induce any additional oxygen vacancies or create any additional oxygen ions and can therefore be considered as a 'stoichiometric' doping mechanism. Oxygen vacancies in the NBT-BA solid solutions are only generated by Bi_2O_3-loss during ceramic processing. Consequently, the oxygen vacancy concentration in the solid solution is not completely controllable and should therefore occur at a randomly low level, which is very unlikely to result in a systematic decrease of conductivity with increasing *x*. Therefore, a significant change in the oxygen vacancy concentration, if there is any, is not the dominant factor for the suppressed oxide-ion conduction in the NBT-BA solid solutions. It is more reasonable therefore to attribute the suppressed oxide-ion conduction on BA incorporation to increased trapping of the residual oxygen vacancies, as discussed below.

Average structure

From general structure considerations, oxide-ion conductivity in a perovskite is often predicted by the following four empirical parameters:

1) Goldschmidt tolerance factor, *t* [34]

$$t = (r_A + r_O)/\sqrt{2}(r_B + r_O), \quad (3)$$

where r_A and r_B are the average ionic size of the A- and B-site cation(s) (12- and 6-fold co-ordination, respectively); r_O is the ionic size of oxygen ion (6-fold co-ordination, r_O = 1.40 Å).

2) The lattice free volume, V_{sf} [35]

$$V_{sf} = (V - \sum V_{ion})/V, \quad (4a)$$

where *V* and V_{ion} are the volume of the unit cell and the volume of each constituent ion, respectively. *V* can be estimated by [36]

$$V = [2.15r_B + 2.72 - 1.40(s-1)]^3, \quad (4b)$$

where

$$s = \sqrt{2}(r_B + r_O)/(r_A^* + r_O), \quad (4c)$$

where r_A* is the ionic radius of the A-site cation in 8-fold co-ordination (not 12).

3) The critical radius, r_C, defined by Kilner and Brook [36]

$$r_C = \frac{a_0(0.75a_0 - \sqrt{2}r_B) - (r_A^2 - r_B^2)}{2(r_A - r_B) + \sqrt{2}a_0}, \quad (5)$$

where a_0 is the pseudo cubic lattice parameter.

4) The average metal-oxygen bond energy, E_b, derived via a Born-Haber cycle [37]

$$E_b = \frac{1}{12m}\left(\Delta H_{A_mO_n} - m\Delta H_A - \frac{1}{n}D_{O_2}\right) + \frac{1}{6m}\left(\Delta H_{B_mO_n} - m\Delta H_B - \frac{1}{n}D_{O_2}\right), \quad (6)$$

where and are the heat of formation of the A_mO_n and B_mO_n oxides, respectively. ΔH_A and ΔH_B are the heat of sublimation of the metals A and B, respectively, and D_{O2} is the oxygen dissociation energy.

The tolerance factor, *t*, describes the lattice distortion in the perovskite structure. A small t represents large lattice distortion and thus is detrimental to oxide-ion conduction.[38] The specific free volume, V_{sf}, describes the free space inside a unit cell and a large V_{sf} is beneficial for migration of oxygen ions. Hayashi *et al.* [35] summarized the electrical conductivity data from literature and found an optimum *t* of 0.96 to obtain maximum conductivity in perovskites. They attributed the maximized conductivity to a compromise between *t* and V_{sf}. The critical radius, r_C, describes the saddle point formed by two A-site and one B-site cations. The larger r_C, the easier it is for oxygen ions to pass through the saddle point. The average metal-oxygen bond energy, E_b, was found to have a linear

View Article Online
DOI: 10.1039/C7TC02510J

relationship with the activation energy for oxygen migration: the smaller absolute E_b, the lower activation energy. [37]

The values of these four parameters of the NBT-BA solid solutions were calculated and listed in Table 3. Thermodynamic data of corresponding oxides and metals used to calculate E_b were obtained from Ref.39. With increasing BA content, V_{sf}, and r_C decrease while t and the absolute value of E_b increase. These are all detrimental to oxide-ion conduction in perovskites. However, it should be noted that the change of these parameters with increasing x is quite small. Such a small change in the average structure is unlikely to result in such a dramatic change in conductivity.

Table 3. Tolerance factor t, specific free volume V_{sf}, critical radius r_C and average metal-oxygen bond energy E_b of $(NBT)_{1-x}(BA)_x$ ($0 \le x \le 0.08$) solid solutions.

x	t	V_{sf}	r_C (Å)	E_b (kJ mol^{-1})
0	0.9841	0.2012	0.9074	-240.24
0.01	0.9845	0.2006	0.9072	-240.33
0.02	0.9848	0.2000	0.9069	-240.43
0.03	0.9851	0.1995	0.9066	-240.52
0.04	0.9855	0.1989	0.9063	-240.61
0.05	0.9858	0.1984	0.9061	-240.70
0.06	0.9862	0.1978	0.9058	-240.79
0.07	0.9865	0.1972	0.9055	-240.88
0.08	0.9869	0.1967	0.9052	-240.97

Local structure

Compared to the average structure, the local structure has a more significant impact on the oxygen ion diffusion in NBT, as revealed by first-principles calculations.[40-42] These calculations showed the lowest energy barriers for oxygen ion migration occur in saddle points between Bi-Bi-Ti ions (0.22 eV), whereas higher barriers are observed for Na-Bi-Ti (0.6 - 0.85 eV) and Na-Na-Ti (1.0 – 1.3 eV) saddle points. Experimentally there is no evidence for long range ordering of the A-site cations in NBT and therefore the Na-Bi-Ti saddle points are considered as the rate-limiting step in the overall oxygen ion migration in NBT. For NBT-BA solid solution, there is no evidence for A-site cation ordering with BA incorporation: no additional XRD peaks or sharpening of Raman peaks were observed. Instead, the peak width of the ~ 135 cm^{-1} band (Na-O vibration) increases with increasing x, as shown in Fig.10. Consequently, the Na-Bi-Ti(Al) saddle points are considered to dominate the energy barrier for oxygen ion migration. As Al^{3+} is much smaller than Ti^{4+} and its polarizability is much smaller, i.e. α_{Al} = 0.79 Å^3 [43] compared to α_{Ti} = 2.93 Å^3 [43], it is more difficult for oxygen ions to pass through the Na-Bi-Al saddle point. With increasing x, the number of Na-Bi-Al saddle points increases and therefore the oxygen ion mobility is decreased. However, as the polarizability of Bi^{3+} (6.12 Å^3 [43]) is much higher than Ti^{4+} and Al^{3+}, local deformation at the saddle point when an oxygen ion is passing through should come mainly from Bi^{3+}. The low polarizability of Al^{3+} may not be the determinant factor for the suppressed conductivity.

To further understand the importance of ionic radius and polarizability of the B-site "dopant", $(NBT)_{1-x}(BiGaO_3)_x$ (BG, x = 0.02, 0.04, 0.06 and 0.08) solid solutions were prepared. NBT-BG shows very similar behaviour as NBT-BA: the bulk conductivity also decreased with increasing x (unpublished results). Ga^{3+} has comparable size (0.62 Å, 6-fold co-ordination) with Ti^{4+}, indicating the ionic size not to be a critical factor.

The decreased mobility of charge carriers can originate from trapping of oxygen vacancies. As also revealed in Ref.41, substitution of Ti^{4+} by acceptor-type dopants (e.g., Mg^{2+}) may significantly increase the oxygen migration barrier due to binding between negatively charged $Mg_{Ti}^{''}$ and positively charged $V_O^{\bullet\bullet}$, even at temperatures > 1000 K. In the case of NBT-BA solid solution, $Al_{Ti}^{'}$ can trap $V_O^{\bullet\bullet}$ to form defect complex $\left(Al_{Ti}^{'}-V_O^{\bullet\bullet}\right)^{\bullet}$, which reduces the mobility of $V_O^{\bullet\bullet}$ and thus decreases the ionic conductivity. The concentration of $Al_{Ti}^{'}$ required to trap all $V_O^{\bullet\bullet}$ for each composition (based on formation of only the defect complex $\left(Al_{Ti}^{'}-V_O^{\bullet\bullet}\right)^{\bullet}$) was estimated by $\left[Al_{Ti}^{'}\right]_{required}=\left[V_O^{\bullet\bullet}\right]/x$ and listed in Table 4. When the BA content is low, i.e., x = 0.01, to trap 0.5% $V_O^{\bullet\bullet}$, 50% of the B-sites must be occupied by Al^{3+}, which is much higher than the actual Al^{3+} occupancy (1%). The possibility of trapping $V_O^{\bullet\bullet}$ is low; therefore the mobility of $V_O^{\bullet\bullet}$ remains high. With increasing BA content, the $\left[Al_{Ti}^{'}\right]_{required}$ decreases significantly and the difference between $\left[Al_{Ti}^{'}\right]_{required}$ and the actual $\left[Al_{Ti}^{'}\right]$ becomes smaller. The possibility of trapping $V_O^{\bullet\bullet}$ becomes higher with increasing x, and consequently the mobility of $V_O^{\bullet\bullet}$ decreases and there is a significant increase in E_a for the bulk conduction across the solid solution. For $x \le 0.06$, $\left[Al_{Ti}^{'}\right]_{required} > \left[Al_{Ti}^{'}\right]$ (based on $\left[V_O^{\bullet\bullet}\right]$ = 0.5%), $V_O^{\bullet\bullet}$ are not fully trapped, therefore there is still a contribution from the oxide-ion conduction and the materials remain as mixed conductors. For x = 0.07 and 0.08, $\left[Al_{Ti}^{'}\right]_{required} \le \left[Al_{Ti}^{'}\right]$, all $V_O^{\bullet\bullet}$ can be trapped by Al^{3+}. This agrees with the $\sigma - x$ and $t_{ion} - x$ relationships as shown in Figure 6 and 8 and with the effective concentration of Al traps available ($\left[Al_{Ti}^{'}\right]_{effective}=\left[Al_{Ti}^{'}\right]/\left[Al_{Ti}^{'}\right]_{required}$) as a function of x, Table 4. Therefore, trapping of $V_O^{\bullet\bullet}$ is a more important factor for the suppressed oxide-ion conduction in the NBT-BA solid solution. Although recent density-functional-theory (DFT) calculations [44] suggest that association of $Mg_{Ti}^{''}$ and $V_O^{\bullet\bullet}$ in Mg-doped NBT is significant only at low temperature range (i.e., < 400 °C), it is possible that $Al_{Ti}^{'}$ has a stronger ability to trap $V_O^{\bullet\bullet}$ as the Al-O binding strength (~ 502 kJ mol^{-1} [45]) is significantly higher than that of Mg-O (358 kJ mol^{-1} [45]) and therefore the $\left(Al_{Ti}^{'}-V_O^{\bullet\bullet}\right)^{\bullet}$ can be stable at higher temperatures.

Pinning of the oxygen vacancies by grain boundaries may be another possibility and/or an additional factor that contributes to the reduced mobility of the oxygen vacancies in the ceramics. Fig.3b shows the grain size decreases with

View Article Online
DOI: 10.1039/C7TC02510J

increasing *x*, therefore the number of grain boundary increases with increasing *x* and consequently a higher chance to pin oxygen vacancies. Grain boundaries have much more complicated defect chemistry than the bulk and therefore need further investigation.

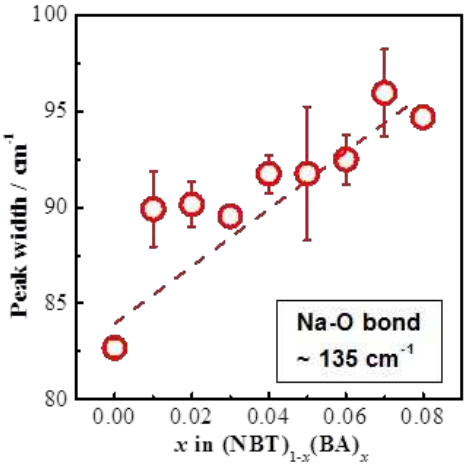

Fig. 10 Peak width of the ~ 135 cm^{-1} band as a function of *x* in $(NBT)_{1-x}(BA)_x$ ($0 \le x \le 0.08$) solid solutions.

Table 4 Concentration of $V_O^{\bullet\bullet}$ (estimated value according to ref. [24]), $Al_{Ti}^{'}$ in $(NBT)_{1-x}(BA)_x$ ($0.01 \le x \le 0.08$) solid solutions, and the concentration of $Al_{Ti}^{'}$ required to trap all $V_O^{\bullet\bullet}$.

x	$[V_O^{\bullet\bullet}]$ (%)	$[Al_{Ti}^{'}]$ (%)	$[Al_{Ti}^{'}]_{required}$ (%)	$[Al_{Ti}^{'}]_{effective}$ (%)
0.01	0.25 – 0.5	1	25 - 50	2 – 4
0.02	0.25 – 0.5	2	12.5 - 25	8 – 16
0.03	0.25 – 0.5	3	8.33 - 16.67	18 – 36
0.04	0.25 – 0.5	4	6.25 - 12.5	32 – 64
0.05	0.25 – 0.5	5	5 - 10	50 – 100
0.06	0.25 – 0.5	6	4.17 - 8.33	72 – 100
0.07	0.25 – 0.5	7	3.57 - 7.14	98 – 100
0.08	0.25 – 0.5	8	3.13 - 6.25	100

Na/Bi ratio

Our previous studies [22, 23] show the electrical conductivity and bulk conduction mechanisms of NBT are highly sensitive to low levels of A-site nonstoichiometry. When Na/Bi ≥ 1, i.e., Na-rich or Bi-deficient, NBT is predominantly an oxide-ion conductor with high σ_b (> 1.0×10^{-3} S cm^{-1} at 600 °C); when Na/Bi < 1, i.e., Bi-rich or Na-deficient, NBT exhibits predominantly electronic conduction with very low σ_b (~ 2.0×10^{-6} S cm^{-1} at 600 °C). As shown in Fig. 11, a dramatic change in bulk conductivity of around three orders of magnitude is observed at the vicinity of Na/Bi = 1 at 600 °C due to this switch in conduction mechanism. The bulk conductivity of the NBT-BA solid solution also shows a dependence on the Na/Bi ratio, Fig. 11. In contrast to the sharp change observed for undoped NBT, a continuous drop of conductivity with decreasing Na/Bi ratio is observed, which is attributed primarily to defect association as mobile $V_O^{\bullet\bullet}$ become increasing trapped with increasing Al-content in the solid solution. This result indicates that a Bi-rich, A-site environment is not necessarily good for the oxide-ion conduction even though the polarizability of Bi^{3+} is high. Trapping of oxygen vacancies by B-site acceptor-type dopants plays a more important role in the oxide-ion conduction of NBT-based material, even at high temperatures.

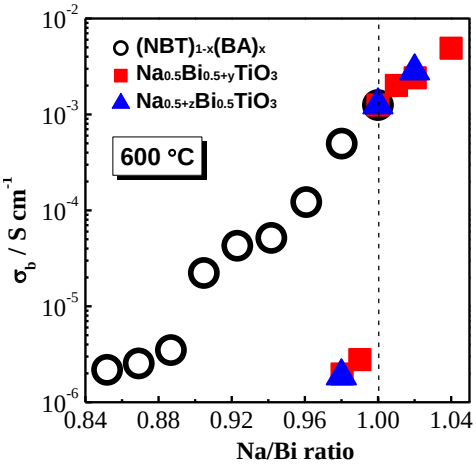

Fig. 11 Effect of A-site Na/Bi ratio on the bulk conductivity of $(NBT)_{1-x}(BA)_x$ ($0 \le x \le 0.08$) solid solutions (this work), $Na_{0.5+y}Bi_{0.5}TiO_3$ (y = -0.01, 0, 0.01) [22] and $Na_{0.5}Bi_{0.5+z}TiO_3$ (z = -0.02, -0.01, -0.005, 0, 0.005, 0.01) [23].

Conclusions

$(NBT)_{1-x}(BA)_x$ ($0 \le x \le 0.08$) solid solutions were prepared by solid state reaction and their electrical properties studied by *ac* impedance spectroscopy and electromotive force transport number measurements. Incorporation of BA decreases the electrical conductivity of NBT and changes the conduction mechanism with increasing x from predominant oxide-ion conduction (type I), to mixed ionic-electronic conduction (type II) and finally to predominant electronic conduction (type III). The suppression of oxide-ion conductivity significantly reduces the dielectric loss at elevated temperatures and consequently transforms the NBT-BA solid solution higher end members into excellent high-temperature dielectric materials. The suppressed oxide-ion conduction with increasing BA content is attributed mainly to a decrease of oxygen vacancy mobility associated with Al acceptor trapping. Although we cannot rule out the influence

of grain boundaries as a source trapping centres, the close correlation between the expected oxygen vacancy concentration and the level of BA doping (see Table 4 for details) provides compelling evidence for an alternative approach to fine tune the electrical conductivity and conduction mechanism of NBT, *viz*. the trapping of oxygen vacancies using B-site acceptor dopants (i.e. Al^{3+}) as opposed to the filling of oxygen vacancies using B-site donor dopants (i.e. Nb^{5+}). This study also reveals the importance of local structure, especially defect association, on the oxide-ion conduction mechanism(s) in NBT-based materials.

Acknowledgements

We thank the EPSRC for funding EP/L027348/1.

References

1 E. Aksel and J. L. Jones, Sensors, 2010, **10**, 1935.
2 D. Damjanovic, N. Klein, J. Lin and V. Porokhonskky, Functional Mater. Lett., 2010, **3**, 5.
3 K. Reichmann, A. Feteira and M. Li, Materials, 2015, **8**, 8467.
4 M. Davies, E. Aksel and J. L. Jones, J. Am. Ceram. Soc., 2011, **94**, 1314.
5 T. Takenaka, K. Maruyama and K. Sakata, Jpn. J. Appl. Phys., 1991, **30**, 2236.
6 T. Wada, K. Toyoike, Y. Imanaka and Y. Matsuo, Jpn. J. Appl. Phys., 2001, **40**, 5703.
7 J. R. Gomah-Pettry, S. Said, P. Marchet, J. P. Mercurio, J. Eur. Ceram. Soc., 2004, **24**, 1165.
8 E. Venkata Ramana, B. V. Bahuguna Saradhi, S. V. Suryanarayana and T. Bhima Sankaram, Ferroelectrics, 2005, **324**, 55.
9 Y. Hiruma, K. Yoshii, H. Nagata and T. Takenaka, Ferroelectrics, 2007, **346**, 114.
10 Y. Hiruma, H. Nagata and T. Takenaka, J. Appl. Phys., 2008, **104**, 124106.
11 R. Selvamani, G. Singh, V. Sathe, V. S. Tiwari and P. K. Gupta, J. Phys: Condens. Matter, 2001, **23**, 055901.
12 H. Yu and Z. Ye, Appl. Phys. Lett., 2008, **93**, 112902.
13 A. Ullah, C. Ahn, K. Jang, A. Hussain and I. Kim, Ferroelectrics, 2010, **404**, 167-172.
14 P. Baettig, C. Shelle, R. LeSar, U. Waghmare and N. Spaldin, Chem. Mater., 2005, **17**, 1376.
15 A. Belik, T. Wuernisha, T. Kamiyama, K. Mori, M. Maie, T. Nagai, Y. Matsui and E. Takayama-Muromachi, Chem. Mater., 2006, **18**, 133.
16 R. V. K. Mangalam, S. V. Bhat, A. Iyo, Y. Tanaka, A. Sundaresan and C. N. R. Rao, Solid State Commun., 2008, **146**, 435.
17 H. Yu and Z. Ye, J. Appl. Phys., 2008, **103**, 034114.
18 Y. Watanabe, Y. Hiruma, H. Nagata and T. Takenaka, Key. Eng. Mater., 2009, **388**, 229.
19 S. Manotham, C. Kruea-In and G. Rujijanagul, Ferroelectrics, 2014, **458**, 152.
20 W. Peng, C. Mao, Z. Liu, X. Dong, F. Cao and G. Wang, Appl. Phys. Lett., 2005, **106**, 092903.
21 M. Li, M. J. Pietrowski, R. A. De Souza, H. Zhang, I. M. Reaney, S. N. Cook, J. A. Kilner and D. C. Sinclair, Nat. Mater., 2014, **13**, 31.
22 M. Li, H. Zhang, S. N. Cook, L. Li, J. A. Kilner, I. M. Reaney and D. C. Sinclair, Chem. Mater., 2015, **27**, 629.
23 L. Li, M. Li, H. Zhang, I. M. Reaney and D. C. Sinclair, J. Mater. Chem. C, 2016, **4**, 5779.
24 M. Li, L. Li, J. Zang and D. C. Sinclair, Appl. Phys. Lett., 2015, **106**, 102904.
25 D. Schütz, M. Deluca, W. Krauss, A. Feteira, T. Jackson, K. Reichmann, Adv. Funct. Mater., 2012, **22**, 2285.
26 M. Bousquet, J. –R. Duclère, E. Orhan, A. Boulle, C. Bachelet and C. Champeaux, J. Appl. Phys., 2010, **107**, 104107.
27 A. C. Larson, R. B. Von Dreele, General Structure Analysis System (GSAS). Los Alamos National Laboratory Report LAUR **1994**, 86-748.
28 B. H. Toby, J. Appl. Crystallogr., 2001, **34**, 210.
29 E. Aksel, J. S. Forrester, B. Kowalski, M. Deluca, D. Damjanovic and J. L. Jones, Phys. Rev. B, 2012, **85**, 024121.
30 M. K. Niranjan', T. Karthik, S. Asthana', J. Pan and U. V. Waghmare, J. Appl. Phys., 2013, **113**, 194106.
31 J. Kreisel, A. M. Glazer, G. Jones, P. A. Thomas, L. Abello and G. Lucazeau, J. Phys.: Condens. Matter, 2000, **12**, 3267.
32 L. Luo, W. Ge, J. Li, D. Viehland, C. Farley, R. Bodnar, Q. Zhang and H. Luo, J. Appl. Phys., 2011, **109**, 113507.
33 O. Chaix-Pluchery and J. Kreisel, Phase Transit., 2011, **84**, 542.
34 V. M. Goldschmidt, T. Barth, G. Lunde, W. Zachariasen, Pt. VII Skrifter Norske Videnskabs-Akademi, Oslo (1926) 117.
35 H. Hayashi, H. Inaba, M. Matsuyama, N. G. Lan, M. Dokiya and H. Tagawa, Solid State Ionics, 1999, **122**, 1.
36 J. A. Kilner and R. J. Brook, Solid State Ionics, 1982, 6, 237.
37 R. L. Cook and A. F. Sammells, Solid State Ionics, 1991, **45**, 311.
38 J. RanlØv, N. Bonanos, F. W. Poulsen and M. Mogensen, Solid State Phenom., 1994, **39-40**, 219.
39 L. V. Guivich, I. V. Beyts and C. B. Alcock, *Thermodynamic Properties of Individual Substances, Fourth Edition*, Vol.3, CRC Press, Boca Raton, FL, 1994.
40 J. A. Dawson, H. Chen and I. Tanaka, J. Mater. Chem. A, 2015, 3, 16574.
41 X. He and Y. Mo, Phys.Chem. Chem. Phys., 2015, **17**, 18035.
42 M. S. Islam, J. Mater. Chem., 2000, **10**, 1027.
43 N. M. Grimes and R. W. Grimes, J. Phys. Condens. Matter, 1998, 10, 3029.
44 K. Meyer and K. Albe, J. Mater. Chem. A, 2017, **5**, 4368.
45 Y. R. Luo, *Comprehensive handbook of chemical bond energies*, CRC Press, Boca Raton, FL, 2007.

View Article Online
DOI: 10.1039/C7TC02519J

Table of contents

- Fine tune the electrical conduction mechanism(s) of NBT-based materials by trapping oxygen vacancies using B-site acceptor dopants.